Available online at www.sciencedirect.com
ScienceDirect
Journal of Hazardous Materials B139 (2007) 220–231
Journal of Hazardous Materials
www.elsevier.com/locate/jhazmat

Arsenic removal by electrocoagulation using combined Al–Fe electrode system and characterization of products

Jewel A.G. Gomes [a], Praveen Daida [a], Mehmet Kesmez [a], Michael Weir [a], Hector Moreno [a], Jose R. Parga [b], George Irwin [c], Hylton McWhinney [d], Tony Grady [d], Eric Peterson [a], David L. Cocke [a,*]

[a] *Gill Chair of Chemistry and Chemical Engineering, Lamar University, P.O. Box 10022, Beaumont, TX 77710, USA*
[b] *Institute Technology of Saltillo, Department of Metallurgy and Materials Science, V. Carranza 2400, C.P. 25280, Saltillo, Coahuila, México*
[c] *Department of Chemistry and Physics, Lamar University, Beaumont, TX 77710, USA*
[d] *Department of Chemistry, Prairie View A&M University, Prairie View, TX 77446, USA*

Received 24 July 2005; received in revised form 28 October 2005; accepted 2 November 2005
Available online 29 September 2006

Abstract

Combination of electrodes, such as aluminum and iron in a single electrochemical cell provide an alternative method for removal of arsenic from water by electrocoagulation. The removal process has been studied with a wide range of arsenic concentration (1–1000 ppm) at different pH (4–10). Analysis of the electrochemically generated by-products by XRD, XPS, SEM/EDAX, FT-IR, and Mössbauer Spectroscopy revealed the expected crystalline iron oxides (magnetite (Fe_3O_4), lepidocrocite (FeO(OH)), iron oxide (FeO)) and aluminum oxides (bayerite ($Al(OH)_3$), diaspore (AlO(OH)), mansfieldite ($AlAsO_4{\cdot}2(H_2O)$), as well as some interaction between the two phases. The amorphous or very fine particular phase was also found in the floc. The substitution of Fe^{3+} ions by Al^{3+} ions in the solid surface has been observed, indicating an alternative removal mechanism of arsenic in these metal hydroxides and oxyhydroxides by providing larger surface area for arsenic adsorption via retarding the crystalline formation of iron oxides.

Keywords: Electrocoagulation; Combined Al–Fe electrode system; Wastewater; Arsenic removal; Ionic substitution

1. Introduction

Arsenic, a toxic trace element present in natural waters (ground and surface water), has become a major unavoidable threat for the life of human beings and useful microorganisms. Arsenic concentration in soils and water can become elevated due to several reasons like, mineral dissolution, use of arsenical pesticides, disposal of fly ash, mine drainage, and geothermal discharge [1]. The major arsenic species present in natural waters are arsenate ions: H_3AsO_4, $H_2AsO_4^-$, $HAsO_4^{2-}$, and AsO_4^{3-} (oxidation state V) and arsenite ions, H_3AsO_3, $H_2AsO_3^-$ and $HAsO_3^{2-}$ (oxidation state III). However, As(V) ions are most prevalent in oxygenated water while As(III) is found in anaerobic conditions like in well water or in groundwater. The concentration of arsenic species is mainly dependent on redox potentials [2] and pH [3]. From the Pourbiax diagram of arsenic [4], it is evident that under low pH and mildly reducing conditions, As(III) is thermodynamically stable and exists as arsenious acid, whereas at oxidizing conditions of low pH, As(V) exists as arsenic acid. Arsenate species are the only species that can exist at high redox potentials on the entire pH range.

Electrocoagulation (EC) is a simple, efficient and promising method where the flocculating agent is generated by electro-oxidation of a sacrificial anode, generally made up of iron or aluminum. In this process, treatment is done without adding any chemical coagulant or flocculant, thus reducing the amount of sludge that must be disposed [5]. A removal efficiency as high as 99% through EC has been reported for the treatment of oil wastes [6,7], dye-containing solutions [8–10], potable water [11], urban and restaurant wastewater [12,13], nitrate or fluoride containing

* Corresponding author. Tel.: +1 409 880 8372; fax: +1 409 880 8374.
E-mail address: cockedl@hal.lamar.edu (D.L. Cocke).

0304-3894/$ – see front matter © 2006 Published by Elsevier B.V.
doi:10.1016/j.jhazmat.2005.11.108

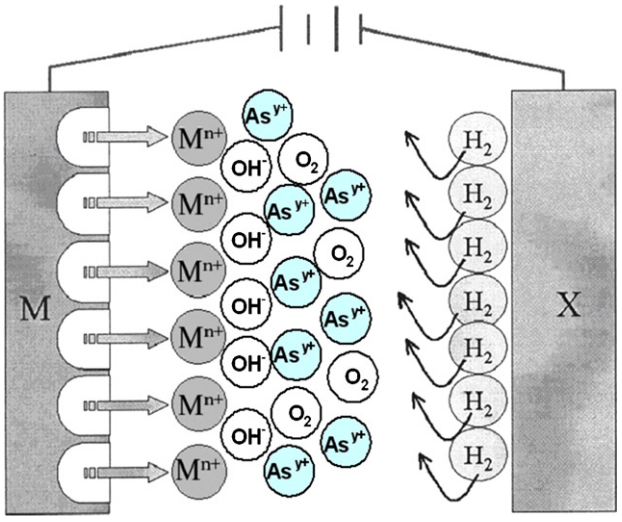

Fig. 1. Conceptual sketch of the electrocoagulation mechanism. M and X indicate electrodes. They may be different or same materials. *n* indicates charge of the metallic ions produced. The arrows indicate the migration of electrolysis gases towards top of the solution.

waters [14,15], and treatment of heavy metal containing solutions [16–21].

In an EC process, the coagulating ions are produced in situ involving three successive stages: (i) formation of coagulants by electrolytic oxidation of the "sacrificial electrode", such as iron or aluminum, (ii) destabilization of the contaminants, particulate suspension and breaking of emulsions, (iii) aggregation of the destabilized phases to form flocs. Fe/Al gets dissolved from the anode generating corresponding metal ions, which almost immediately hydrolyze to polymeric iron or aluminum oxyhydroxides. These polymeric oxyhydroxides are excellent coagulating agents. Fig. 1 shows a conceptual sketch of the electrocoagulation mechanism. As shown in Fig. 1, the anodic reaction involves the dissolution of metal, and the cathodic reaction involves the formation of hydrogen gas and hydroxide ions [1].

For example, Al^{3+} ions on hydrolysis may generate the aqueous complex $Al(H_2O)_6^{3+}$, which is predominant at pH < 4. As the pH (and/or temperature) increases, the hydrated trivalent aluminum ion undergoes hydrolysis, initially forming the $Al(OH)(H_2O)_5^{2+}$ ion and then hydroxyaluminum species, such as $Al(OH)_2^+$, $Al(OH)_3$ (insoluble), $Al(OH)_4^-$, $Al_2(OH)_2^{4+}$, and $Al(OH)_5^{2-}$, and eventually hydroxy polymers such as $Al_{13}(OH)_{32}^{7+}$ [22]. Between pH 5 and 6 the predominant hydrolysis products are $Al(OH)^{2+}$ and $Al(OH)_2^+$; between pH 5.2 and 8.8 the solid $Al(OH)_3$ is most prevalent; and above pH 9 the soluble species $Al(OH)_4^-$ is the predominant and the only species present above pH 10. Throughout the pH gradient (pH 4.7 and 10.5), the presence of polymeric aluminum hydroxides would provide significantly larger surface areas for arsenic species adsorption due to their amorphous nature.

Ferric ions generated by electrochemical oxidation of iron electrode may form monomeric species, $Fe(OH)_3$ and polymeric hydroxy complexes namely, $Fe(H_2O)_6^{3+}$, $Fe(H_2O)_5(OH)_2^+$, $Fe(H_2O)_4(OH)_2^+$, $Fe_2(H_2O)_8(OH)_2^{4+}$ and $Fe_2(H_2O)_6(OH)_4^{4+}$ depending on the pH of the aqueous medium. These hydroxides/polyhydroxides/polyhydroxyoxide metallic compounds have strong affinity for dispersed particles as well as counter ions to cause coagulation. In addition, both the As(V) and As(III) were shown to be strongly sorbed by iron(III) oxides such as amorphous $Fe(OH)_3$, hydrous ferric oxide (HFO) and goethite (FeO(OH)) [23,24]. Arsenate anion bound to HFO can form common naturally occurring arsenate minerals $FeAsO_4{\cdot}2H_2O$ (scorodite) and $Fe_3(AsO_4)_2{\cdot}8H_2O$ (symplesite) as the dominant solid phase [25]. Therefore, arsenic is removed by iron species either by compound formation or by surface complex adsorption or both.

The sacrificial metal anodes are used to continuously produce polymeric oxyhydroxides in the vicinity of the anode. Coagulation occurs when these metal cations combine with the negative particles carried towards the anode by electrophoretic motion. Contaminants present in the wastewater stream are treated either by chemical reactions and precipitation or physical and chemical attachment to colloidal materials being generated by the electrode erosion. They are then removed by electroflotation, or sedimentation and filtration. Thus, rather than adding coagulating chemicals as in conventional coagulation process, these coagulating agents are generated in situ.

EC with aluminum and iron electrodes was patented in the US in 1909. The electrocoagulation of drinking water was first applied on a large scale in the US in 1946 [26,27]. Electrocoagulation using Fe–Fe electrodes [19,20,28–32] and Al–Al electrodes [11,13,33–36] system has already drawn a considerable attention in previous research. According to our literature survey, only a very few reports on the combined use of both aluminum and iron in the same EC cell has been published [37–40]. They used aluminum as sacrificial anode and stainless steel or iron as cathode for removal of carbon black, clay, and suspended solids without changing polarity of electrodes. The use of combination electrodes of dissimilar metals and the frequent change of their polarity has not yet been studied, which may provide an alternative method for efficient removal of both organic materials and heavy metals from water. In the present work, we report on arsenic removal efficiency of the Al–Fe combination electrode system and the characterization of the EC by-products using Powder X-ray diffraction (PXRD), X-ray photoelectron spectrsocpy (XPS), scanning electron miscroscopy (SEM)/energy dispersive spectroscopy (EDS), Fourier transform infrared (FT-IR), and Mössbauer spectroscopy.

2. Experimental

2.1. Reagents

The electrodes used in this study consisted of aluminum plates (30 mm × 20 mm × 0.5 mm) and iron plates (50 mm × 25 mm × 0.5 mm). All chemicals were of analytical grade and supplied by Aldrich. Stock arsenic solutions of 1.32 g/l were prepared according to the EPA standard method by dissolving arsenic oxide (As_2O_3) in 20% (v/v) potassium hydroxide and then neutralizing by 20% (v/v) sulfuric acid to a phenolphthalein end point and then diluting to 1 l with 1% (v/v) sulfuric

acid. Solutions of lower concentrations were prepared by proper dilution. The pH of the solution was adjusted by adding either sodium hydroxide or sulfuric acid.

All measurements were carried out at ambient temperature ($25 \pm 1\,^{\circ}C$), on 200 ml aliquot of arsenic solution added with the same amount of sodium chloride (0.8 g) to avoid excessive ohmic drop and to prevent the formation of the passivation layer on aluminum electrodes. The addition of chloride salts decreased the energy consumption and limits the temperature variations, due to the Joule effect [41].

Electrocoagulation was conducted at: (i) different residence time, (ii) at different pH, (iii) at different current density, and (iv) at different initial concentrations (1–1000 ppm of As(III)) using three combinations of electrodes (Al–Al, Fe–Fe, and Al–Fe). The polarity of the electrodes were reversed every 15 min. The solution was constantly stirred using a magnetic stirrer to reduce the mass transport overpotential of the EC cell.

2.2. Electrocoagulation procedure

Electrocoagulation was carried out in a 250 ml beaker with magnetic stirrer, using vertically positioned aluminum and/or iron electrodes spaced by 30 mm and dipped in the wastewater. The experimental set-up is presented in Fig. 2. The current and voltage during the EC process were checked using Cen-Tech multimeters. The current density was 3–30 mA/cm^2. The pH of the solutions before and after EC was measured by an Oakton pH meter.

EC was run for a certain period of time (either 1 or 2 h). After that, the EC-mixture was filtered and the precipitate was dried and weighed. The solid precipitate was characterized by FT-IR, PXRD, XPS, SEM/EDS, and Mössbauer spectroscopy. The filtrate was used for determining the amount of residual arsenic.

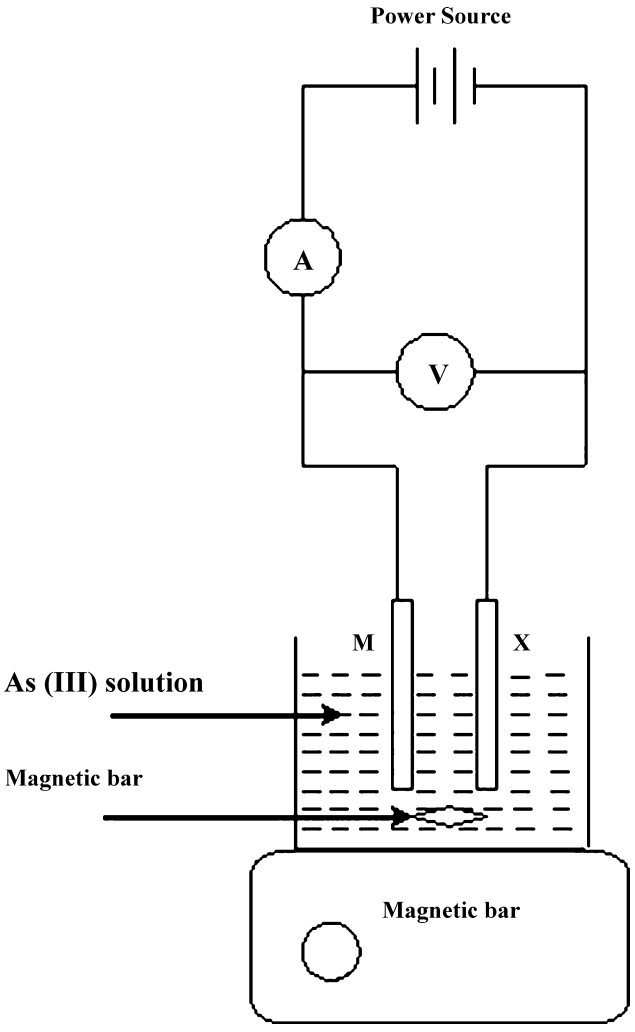

Fig. 2. Experimental set-up for arsenic removal using electrocoagulation system. M and X represent the electrode materials (Al–Al, Fe–Fe or Al–Fe). Every 15 min the polarity of the electrodes were reversed.

2.3. Methods of analysis

2.3.1. Inductively coupled plasma-atomic emission spectrometry (ICP-AES)

The filtered and feed solutions were analyzed by Earth Analytical Sciences, Inc. using method SW846_6010 B (ICP-AES) with a lower detection limit of 50 or 100 ppb.

2.3.2. Fourier transform infrared spectroscopy

FT-IR analysis were carried out by Thermonicolate FT-IR spectrometer and OMNIC software using potassium bromide pellets (sample: KBr = 1: 50). The spectra were recorded in the range of 4000–400 cm^{-1} with 2 cm^{-1} resolution. A 32 scans were collected for each specimen.

2.3.3. Powder X-ray diffraction

The PXRD analysis of the electrocoagulation by-products were carried out with a Bruker AXS D4 Endeavor diffractometer operating with a Cu Kα radiation source filtered with a graphic monochromator (λ = 1.5406 Å). The samples were ground to a fine powder by wet grinding method using methanol 99.8% from Sigma–Aldrich and loaded into a sample holder. Powder specimens were filtered with 400 mesh sieves preceding the X-ray diffraction analysis. The XRD scans were recorded from 15 to 75° 2θ with 0.020° step-width and 6 s counting time for every step.

2.3.4. X-ray photoelectron spectroscopy

XPS studies were carried out on material which was electrodeposited under various conditions. A PHI 5600 XPS utilizing Mg Kα X-ray at 1487 eV, 10^{-9} Torr, 300 W was used to examine the particulate material. The adventitious carbon peak at 284.6 eV was used as an internal standard to shift all photoelectron lines to their correct binding energies.

2.3.5. Scanning elecron microscope and energy dispersive X-ray analyzer

EC-byproducts were analyzed by a JEOL-6400 scanning electron microscope (SEM). The elemental composition of the materials was determined by energy dispersive analysis of X-rays (EDAX) (Oxford Inca) and referenced against O, Na, Al, S, Cl, K, Fe, Co, and As standards.

2.3.6. Mössbauer spectroscopy

$_{57}$Fe Mössbauer measurements were obtained using a $_{57}$Co source in Rh matrix, at ambient temperature, driven in the triangle mode. Results were least-squares fitted using Voigt line shapes, with shifts referenced to α-Fe. The instrumental broadening was small (less than 0.05 mm/s), as estimated from a sodium nitroprusside calibration sample; the reported linewidths were corrected for this term.

3. Results and discussion

3.1. Arsenic removal

The ICP-AES analysis (Table 1) for feed and filtrate solutions after EC process showed that more than 99.6% of arsenic was removed by using Fe–Fe electrode pair. The removal efficiency varied from 78.9% to more than 99.6% at different initial arsenic concentrations (1.42–1230 ppm) when Al–Fe electrode pair was used. On the other hand, by using Al stand alone removal efficiency did not exceed 97.8% after 1 h residence time.

So, it can be concluded that either Fe–Fe or combination of Fe and Al plates as sacrificial electrodes in EC process is very promising for arsenic removal. ICP-AES analysis results also demonstrated that the increase in residence time improves the arsenic removal efficiency as shown in Fig. 3 for the case of Al–Al electrode-pair. According to a report of Masue et al. [42], strong retention of arsenic was observed at the pH ranges 3–7 with ferrihydrite and its Al-substituted analogs. Fig. 4 shows the effects of pH on the removal efficiency of As using an Al–Fe electrode pair at two wide different concentration range (1.42 and 123.0 ppm) and the initial pH 6 was found to be the optimum pH for maximum arsenic removal. The reason for this

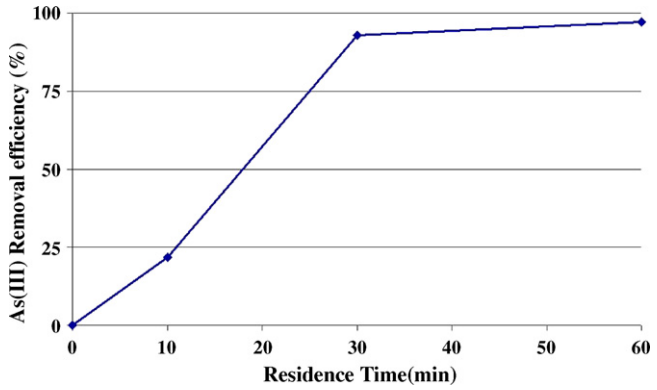

Fig. 3. Removal efficiency of arsenic at different residence times using Al–Al electrode system.

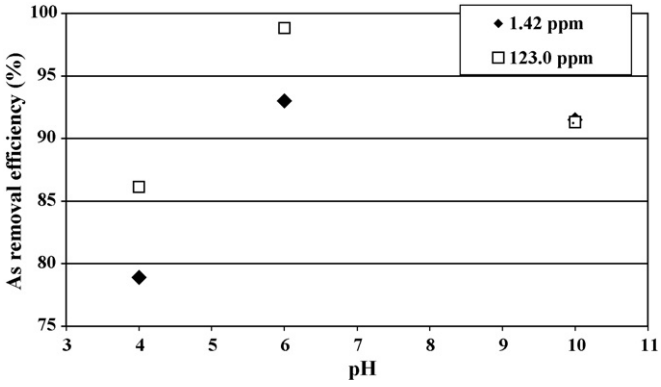

Fig. 4. Arsenic removal efficiency at different pH using Al–Fe electrode system.

Table 1
ICP-AES analysis results for EC filtrates using the method of analysis SW846_6010 B (an EPA analytical method for identification of trace elements by ICP-atomic emission spectrometry)

Electrode pair	pH	Arsenic concentration (ppm)		Removal efficiency (%)	Residence time (min)	Current density (mA/cm^2)
		Initial	Final			
Al–Fe	4	1.42	0.30	78.9	60	30
		13.4	<0.05	>99.6	60	30
		123.0	17.1	86.1	60	30
		1230	129	89.5	60	30
	6	1.42	<0.10	>93.0	60	30
		123.0	1.43	98.8	60	30
	10	1.42	0.12	91.5	60	30
		123.0	10.7	91.3	60	30
Fe–Fe	2.4	13.4	<0.05	>99.6	60	30
		13.4	<0.05	>99.6	120	3
Al–Al	2.4	13.4	10.5	21.6	10	30
		13.4	0.94	93.0	30	30
		13.4	0.37	97.2	60	30
		13.4	0.09	99.3	120	3
	4	13.4	0.29	97.8	60	30
	6	13.4	0.34	97.5	60	30

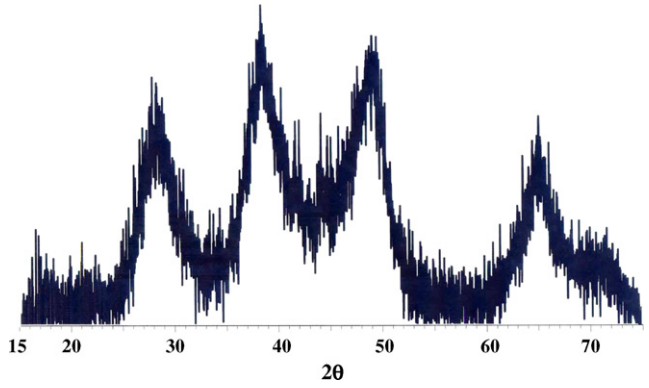

Fig. 5. X-ray diffraction analysis of Al–Al electrode by-product.

observation is not yet clear. We assume that at lower or higher pH, the rate of formation of metal–arsenate/arsenite complexes may be lower due to solubility effects than that at pH 6. We will explore this matter in our future research.

3.2. Material characterization

3.2.1. XRD characterization of electrode by-products

X-ray diffraction spectrum of Al–Al electrode by-product (Fig. 5) showed very broad and shallow diffraction peaks. Bragg reflections possessing very broad humps and low intensity indicate that the analyzed phase possesses a short-range order, i.e., amorphous or very poorly crystalline in nature. From FT-IR analysis of the Al electrode by-product, it is concluded that the chemical speciation of this amorphous phase can be aluminum hydroxide and/or aluminum oxyhydroxide (see Fig. 13, for Al–Al electrode spectrum). Because crystallization of Al hydroxides/oxyhydroxides is a very slow process, most Al hydroxides and aluminum oxyhydroxides found to be either amorphous or very poorly crystalline [43]. Because of their short-range order, these hydroxides/oxyhydroxides gave broad, diffuse XRD peaks, making them very difficult to identify. However, the previous literature on the amorphous nature of aluminum oxide layer [44] supported this result by reporting that the oxide film does not contain a pure crystalline aluminum compound, but contains an amorphous aluminum compound. According to research on barrier-type films, the alumina in this film has been reported as γ′-alumina. The γ′-alumina has properties that lie between amorphous alumina and crystalline alumina. It has also been reported that H and H_2O are connected to a part of the cyclic compound consisting of aluminum atoms and oxygen atoms, forming cyclic aluminic acid trihydrate. According to other research reports, the structure of this cyclic compound is similar to the crystalline structure of As_2O_6, and similar to the spinel structure of Fe_3O_4.

Fe–Fe electrode by-product showed both the well crystalline phases such as magnetite, and the poorly crystalline phases such as iron oxyhydroxides and lepidocrocite (Fig. 6). The presence of poorly crystalline phases of iron oxyhydroxides were verified from the FT-IR analysis of the by-product of Fe electrode, as shown in Fig. 13 (FT-IR spectrum of Fe electrode) and Table 3.

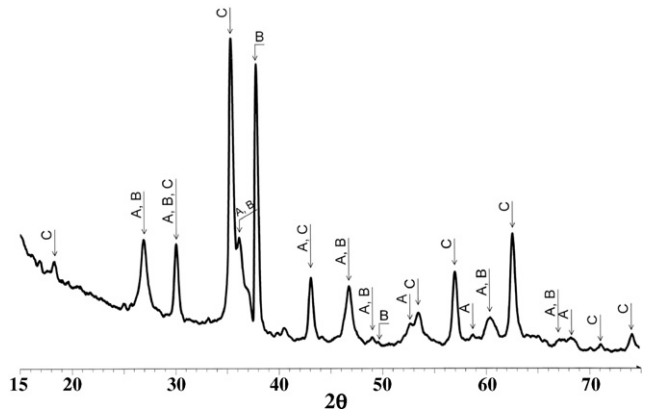

Fig. 6. X-ray diffraction analysis of Fe–Al electrode by-product (iron hydroxide oxide: A, lepidocrocite: B, magnetite: C). The *y*-axis indicates relative X-ray intensity in no. of counts.

Combined Fe and Al electrodes in a single EC reactor demonstrated amorphous/poorly crystalline phases for aluminum hydroxide/oxyhydroxides and arsenate (bayerite ($Al(OH)_3$), diaspore (AlO(OH)), mansfieldite ($AlAsO_4{\cdot}2(H_2O)$)), and iron oxyhydroxides (lepidocrocite (FeO(OH)), magnetite (Fe_3O_4), iron oxide (FeO)) as shown in Fig. 7. Comparison of diffractograms of Fe–Fe and Al–Fe electrode by-products showed that there is a drastic decrease in the crystallinity of magnetite and lepidocrocite, i.e., the sharp decrease in intensity of the major intense Bragg reflection for the magnetite and lepidocrocite phase at ca. 35–38° 2θ, and also other reflection peaks for these phases were found to be very broad and shallow. Reason for the decrease of magnetite and lepidocrocite crystallinity may be due to the ionic substitution of iron by aluminum. The decrease in crystallinity of lepidocrocite during Al–Fe EC process is probably due to the formation of mansfieldite. Mansfieldite has the similar orthorhombic-dipyramidal crystal system with lepidocrocite and the isomorphic ionic substitution between them may be possible. Table 2 lists the phases identified in EC products using Al–Al, Fe–Fe, and Al–Fe electrode pairs via PXRD, with their corresponding PDF numbers, and their most likely nature.

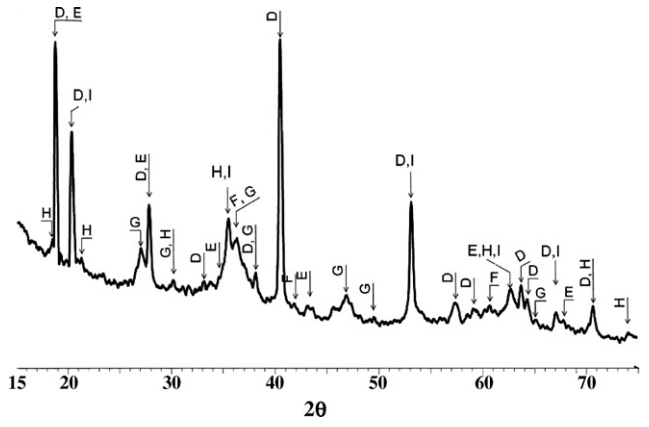

Fig. 7. X-ray diffraction analysis of combined Al–Fe electrode by-product (bayerite: D, diaspore: E, iron oxide: F, lepidocrocite: G, magnetite: H, Mansfieldite: I). The *y*-axis indicates relative X-ray intensity in no. of counts.

Table 2
Phases identified in Al, Fe, and combined Al–Fe electrodes' EC by-products via XRD, their corresponding PDF numbers, and most likely nature of the identified phases

Type of electrode(s)	Phases identified or most likely to be present in the by-product	JCPDS-ICDD PDF#
Aluminum	Aluminum hydroxide	–
	Aluminum oxyhydroxide	–
Iron	Iron hydroxide oxide	70–0713
	Lepidocrocite	44–1415
	Magnetite	79–0416
	Magnetite	88–0315
Combined iron–aluminum	Bayerite	83–2256
	Diaspore	88–2351
	Iron oxide	77–2355
	Lepidocrocite	74–1877
	Magnetite	75–1609
	Mansfieldite	23–0123

The identification of all compounds was confirmed by computer-aided search of the PDF Database obtained from The Joint Committee on Powder Diffraction Standards-International Centre for Diffraction Data (JCPDS-ICDD).

3.2.2. XPS studies

The arsenic signal (As3d) for material deposited from 100 ppm (and less) arsenic solution was very weak and in most cases non-existent. All other photoelectron lines (Al2p, Fe2p, and S2p) were detected down to 1 ppm arsenic concentration in solution. Iron appears to exist as Fe^{3+} in all species, as shown in Fig. 8. The iron signal appears at ~711.5 eV, which is typical of iron oxy-hydroxides. The peaks are generally broad and may comprise of multiple iron species [45,46].

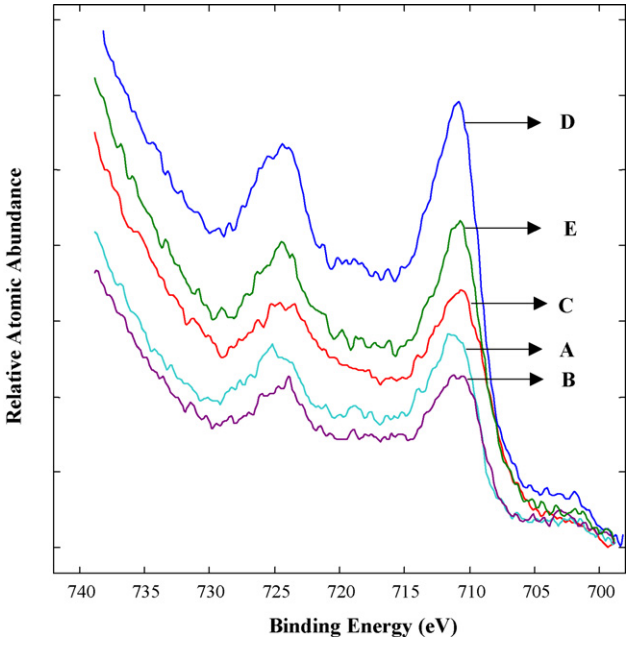

Fig. 8. XPS spectra of (Fe2p) region of electrodeposited material containing arsenic species under various treatment conditions: (A) EC-byproducts of 1 ppm As using Al–Fe electrode system; (B) EC-byproducts of 100 ppm As using Al–Fe electrode system; (C) EC-byproducts of 10 ppm As using Al–Fe electrode system beginning with Al corrosion; (D) EC-byproducts of 10 ppm As using Fe–Al electrode system beginning with Fe corrosion; (E) blank EC-byproducts using Al–Fe electrodes.

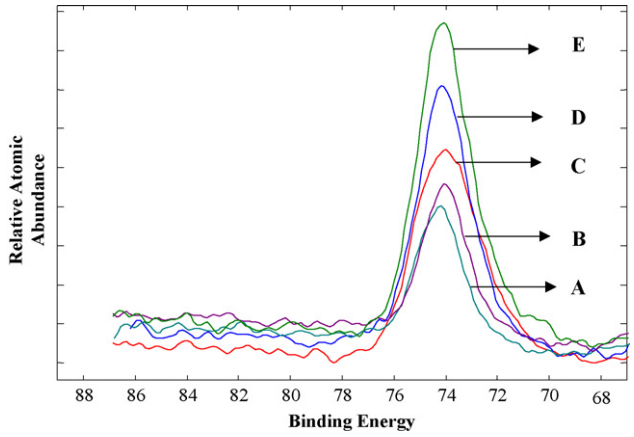

Fig. 9. XPS spectra of (Al2p) region of electrodeposited material containing arsenic species under various treatment conditions: (A) EC-byproducts of 1 ppm As using Al–Fe electrode system; (B) EC-byproducts of 100 ppm As using Al–Fe electrode system; (C) EC-byproducts of 10 ppm As using Al–Fe electrode system beginning with Al corrosion; (D) EC-byproducts of 10 ppm As using Fe–Al electrode system beginning with Fe corrosion; (E) blank EC-byproducts using Al–Fe electrodes.

Aluminum at ~74 eV is typical of Al oxide–oxyhydroxide spectra as shown in Fig. 9. Sample A contained the EC-byproduct from 1 ppm As solution and sample E contains blank EC-byproduct. (Al2p) peaks for these two spectra coincide with each other. Conversely, the peak is slightly shifted towards lower binding energy for the EC-byproduct of 100 ppm As (sample B). Samples C and D, which contain EC-byproducts of 10 ppm As, the peaks lie between these two extremes. This implies that As is adsorbed on the surface of the EC-product and as more As is present in the material, the more it shields the (Al2p) electron and increases the amorphousity of the material, resulting in lower binding energy as seen in the XPS peak. These are the preliminary data. We will explore it more extensively in our future research.

Neither the (Al2p) nor the (Fe2p) spectra (Figs. 8 and 9) indicate that there are any major differences in the chemistry of the respective species. On the other hand, the (As3d) signal (Fig. 10, with 1000 ppm arsenic solution) shows two distinctive fitted peaks at 44.5 and 46.7 eV, corresponding to the As^{3+} and As^{5+}, respectively [47,48]. These are not spin doublets. The energy separation between ($As3d_{5/2}$) and ($As5d_{3/2}$) doublets is approximately 0.7 eV, which results in a convoluted spectrum at the resolution of the instrument.

Results from XPS studies indicate that although the EC experiments were performed with As(III), during the EC process, As(III) was partly converted to As(V). It can also be inferred that at higher concentration, As(III) ion itself can be removed from the wastewater by adsorbing on the floc without changing its oxidation state.

3.2.3. SEM/EDAX

Figs. 11 and 12 show the SEM image and the EDAX spectrum, respectively, of the EC-byproducts containing initial As of 100 ppm at initial pH of 6 with the Al–Fe electrode system. The SEM image indicates the presence of mostly amorphous or ultrafine particular structure at μm size on

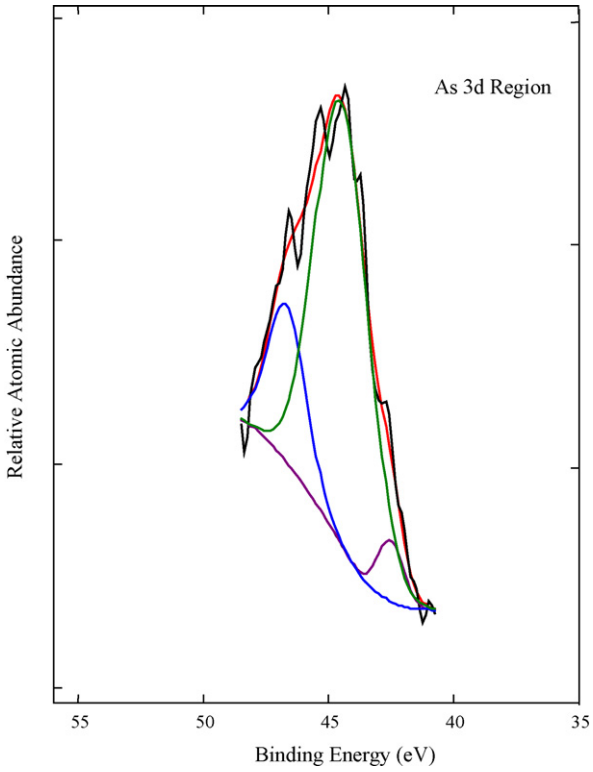

Fig. 10. XPS spectra of (As3d) region of electrodeposited material containing arsenic species under various treatment conditions. A least two oxidation state of arsenic are identified (As^{3+} and As^{5+} at 44.5 and 46.7 eV, respectively). The sample used for this experiment contains EC-byproducts of 1000 ppm As using Al–Fe electrode system.

the surface. The elemental analysis by EDAX confirmed the presence of As removed (0.44 at.%) from the sample solution. It also reveals that the at.% ratio between Al and Fe is 4:5. Other elements detected in the floc comes from the adsorption of the conducting electrolytes, chemicals used in the experiments and the scrap impurities of the Al and Fe electrodes.

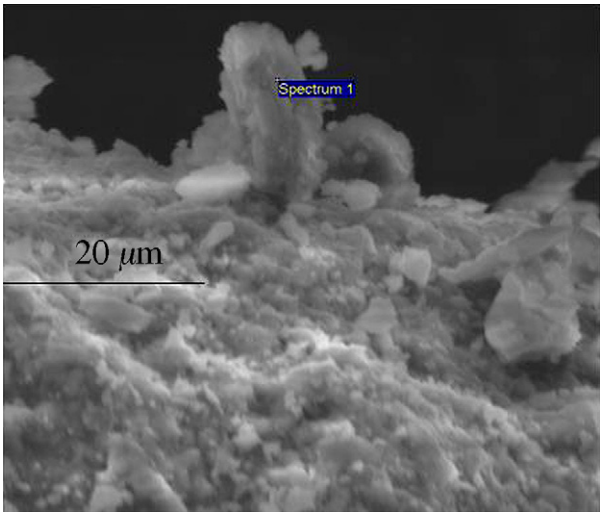

Fig. 11. SEM image of the EC-byproducts containing initial As of 100 ppm at initial pH of 6 with the Al–Fe electrode system. The printing of "Spectrum 1" in this figure indicates the corresponding EDAX spectrum as presented in Fig. 13.

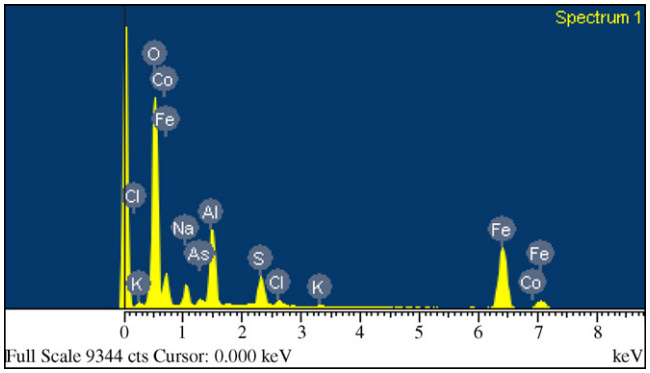

Fig. 12. EDAX spectrum of the EC-byproducts containing initial As of 100 ppm at initial pH of 6 with the Al–Fe electrode system.

3.2.4. FT-IR characterization

FT-IR spectrum of Al-electrode by-product (Fig. 13, Al–Al electrodes) showed, OH stretching, hydroxyl bending, Al–O–H bending and As(III)–O on aluminum hydroxide/oxyhydroxides at ca. 3452, 1638, 926, and 620 cm^{-1}, respectively.

Iron electrode by-product (Fig. 14, Fe–Fe electrodes) showed OH stretching at 3738 and 3447 cm^{-1}, hydroxyl bending and γ'(OH) water bending vibration or overtones of hydroxyl bending around 1637 cm^{-1} [49,50]. Bands for lepidocrocite phase showed up at 1120, 1023, and 745 cm^{-1} [51]. Magnetite (Fe_3O_4 or $Fe_{3-x}O_4$) band at 575 cm^{-1} and Fe–O vibration band is seen at 469 cm^{-1} [51,52].

FT-IR analysis of the by-product of the combined Al–Fe electrodes suggested the presence of several hydroxyl groups

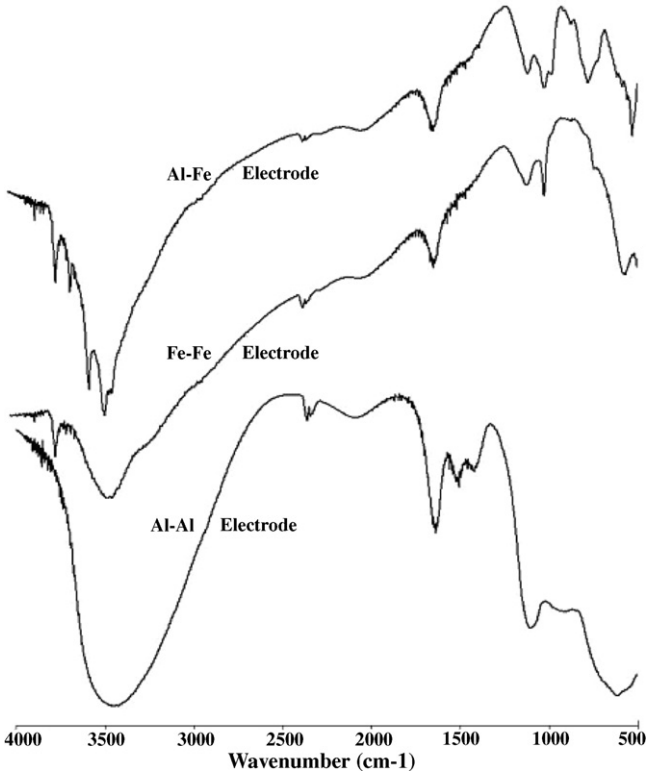

Fig. 13. FT-IR spectra of the solid EC by-products using Al–Fe, Fe–Fe, and Al–Al electrode system. The *y*-axis indicates relative transmittance.

Table 3
FT-IR vibrations and their corresponding wavenumbers and region for the bands observed

Type of electrode	Type of vibrations	Vibration wavenumbers (cm^{-1})	Vibration range (cm^{-1})
Aluminum	OH stretching	3452	3000–3800
	Hydroxyl bending	1638	1572–1813
	Al–O–H bending	926	880–1000
	As(III)–O	620	500–800
Iron	OH stretching	3738	3689–3787
		3447	3550–3000
	Hydroxyl bending	1637	1572–1813
	γ'(OH) water bending	1637	1572–1813
	Overtones of hydroxyl bending	1637	1572–1813
	Magnetite (Fe_3O_4 or $Fe_{3-x}O_4$)	575	526–840
	Fe–O	469	416–510
	Lepidocrocite	1120	1090–1245
		1023	923–1057
		745	730–790
Combined aluminum–iron	OH stretchings for basic hydroxyl groups from aluminum	3549	3530–3644
	hydroxide/oxyhdroxide	3660	3644–3693
		3856	–
	OH stretchings for hydroxyl groups from iron oxyhdroxide	3463, 3439, 3424	–
	γ'(OH) water bending	1637	1572–1813
	Overtones of hydroxyl bending	1637	1572–1813
	Hydroxyl bending	1637	1572–1813
	As(III)–O	795	–
	As(V)–O	874	–
	Lepidocrocite	1120	1090–1245
		1023	923–1057

(see Fig. 13, Al–Fe electrode). Basic hydroxyl groups and their corresponding OH stretching were identified 3549, 3660, and 3736 cm^{-1} for aluminum hydroxide/oxyhydroxides phases [49,53]. Hydroxyl groups corresponding to the iron oxyhydroxides were seen at 3463, 3439, and 3424 cm^{-1}. Hydroxyl bending and γ'(OH) water bending vibration or overtones of hydroxyl bending identified around 1637 cm^{-1} and lepidocrocite bands phase showed up at 1120, 1023 cm^{-1}. As(III)–O vibration at 795 cm^{-1} and As(V)–O at 874 cm^{-1} were observed [49]. Table 3 shows all the identified IR-active vibrations with their corresponding wave numbers.

3.2.5. *Characterization by Mössbauer spectroscopy*

The Mössbauer spectra of three samples were analyzed for hyperfine parameters (isomer shifts, quadrupole splittings, hyperfine magnetic fields, and line broadenings) using a least-squares procedure:

- Sample 1: blank EC in Fe–Fe.
- Sample 2: As-EC in Fe–Fe.
- Sample 3: As-EC in Al–Fe.

The Mössbauer spectra for sample 1 consisted of primarily a doublet, with a weak contribution due to a magnetic sextet spectrum. Sample 2 consisted of a similar doublet spectrum, with a much larger contribution of the magnetic component compared with sample 1. Sample 3 consisted of entirely a doublet, with no apparent magnetic component.

The spectra were fit using a least-squares procedure using routines after Bevington [54] based on the method of Marquardt [55]. Spectra were fitted using line-shape functions consisting of a Lorentzian function convoluted with a Gaussian function (known as Voigt line-shapes). The Gaussian broadening allowed instrumental broadening to be incorporated. Gaussian line-widths were relatively small compared with the natural Lorentzian width of 0.1946 mm/s, suggesting the broadening effects in the spectra primarily were due to increased Lorentzian widths. Also, the outer lines in the six-line magnetic spectra were broadened more than the inner lines, which can be due to inhomogeneous distributions of hyperfine magnetic fields, or more likely due to relaxation effects. Super-paramagnetic relaxation due to fine particle effects was probably the main source of line broadening in the magnetic spectra.

The magnetic contribution to the spectra was consistent with magnetite/maghemite, and sample 1 was analyzed by assuming the electric and magnetic hyperfine parameters were that of magnetite, and the line widths and subspectra intensities (i.e., for the A and B sites in the magnetite structure) extracted through the least-squares fitting procedure. To limit the number of free parameters, it was assumed that Lorentzian broadening of the magnetic lines was a linear function of the magnetic line-shifts, so that outer lines were broadened more than the inner lines.

In the following a brief description of the Mössbauer spectra of magnetite/maghemite is presented [56]. Magnetite has the structural formula:

$$(Fe^{3+})_A \cdot [(Fe^{2.5+})_2]_B O_4$$

where A sites (tetrahedral) are occupied by ferric ions, and on the B sites (octahedral) ferric and ferrous ions have merged into

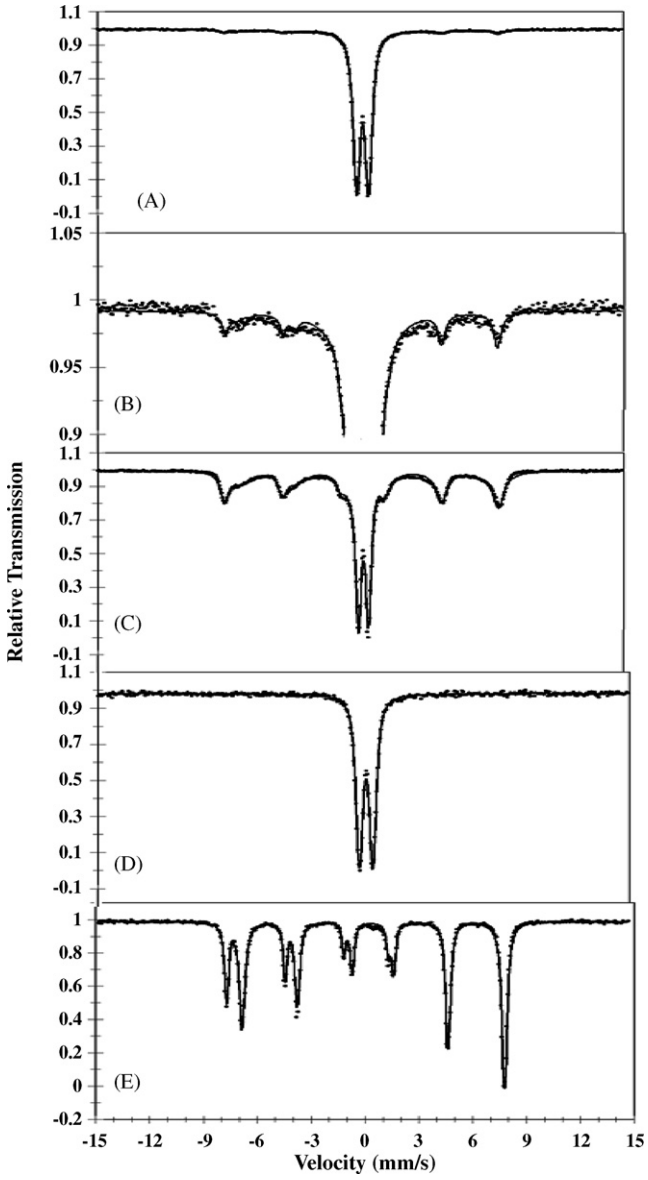

Fig. 14. Mössbauer spectra of the EC by-products: (A) blank EC by-products using Fe–Fe electrode pair; (B) magnified spectrum of A; (C) EC by-products using Fe–Fe electrode pair; (D) EC by-products using Al–Fe electrode pair; (E) pure magnetite.

$Fe^{2.5+}$ by fast electron hopping above the Verwey transition at 125 K. Non-stoichiometric magnetite has the formula:

$$Fe_{3-x}O_4,\ 0 < x < 0.33$$

and fast electron hopping results in the following structural formula:

$$(Fe^{3+})_A \cdot [(Fe^{2.5+})_{2(1-3x)} \cdot (Fe^{3+})_{5x} \cdot \square_x]_B O_4$$

where the vacancies are supposed to be on the octahedral sites. As the endpoint of non-stoichiometric magnetite ($x = 0.33$), maghemite has the general formula:

$$(Fe^{3+})_A \cdot [(Fe^{3+})_{5/3} \cdot \square_{1/3}]_B O_4$$

in which both A and B sites are occupied by Fe^{3+} ions.

The corresponding Mössbauer spectrum of non-stoichiometric magnetite consists in general of a superposition of three magnetic sextets, corresponding to $(Fe^{3+})_A$, $(Fe^{3+})_B$, and $(Fe^{2.5+})_B$. Now the hyperfine parameters for $(Fe^{3+})_A$ and $(Fe^{3+})_B$ are usually very similar, resulting in essentially a single sextet spectrum. The spectrum corresponding to $(Fe^{2.5+})_B$ has much different hyperfine parameters. There are also two sextets for these sites, corresponding to different directions of the electric field gradient, with a single sextet is being generally adequate. In the analysis of the spectra, the $(Fe^{3+})_A$ and $(Fe^{3+})_B$ sites are indicated as sites I, and the $(Fe^{2.5+})_B$ sites are indicated as sites II. For the case of stoichiometric magnetite ($x = 0.0$) I sites are identical with A sites (tetrahedral), and II sites are identical with B sites (octahedral).

Note that the Mössbauer spectra cannot distinguish between magnetite/maghemite mixtures and non-stoichiometric magnetite, and so intensity ratios for the I and II sites cannot be used to determine a composition x, nor can the effects of Al substitution be determined from the hyperfine parameters [56].

Fig. 14A shows the spectrum and results of the least-squares fitting procedure for sample 1. Fig. 14B shows the same spectrum magnified to enhance the magnetic lines. The areas under the doublet and magnetic sextet compared with total area were determined. Table 1 shows the parameters extracted from the procedure.

Fig. 14C shows the spectrum for sample 2. Sample 2 shows a similar magnetic component as in sample 1, but much more intense compared with the doublet. Here a similar procedure was used as for sample 1, but the hyperfine magnetic fields on I and II sites were allowed to be free parameters (the electric hyperfine parameters were assumed as for magnetite). Also, the three sets of magnetic lines for both I and II sites were allowed to have independent values (it was assumed that line 1 and 6 had the same width, lines 2 and 5 had the same width, and lines 3 and 4 had the same width). The resulting hyperfine magnetic fields (see Table 4) were found to be identical with that of magnetite/maghemite. As was assumed for sample 1, the Lorentzian linewidths of the outer lines were greater than the inner lines. As in sample 1, the areas under the doublet and magnetic sextet compared with total area were determined.

Fig. 14D shows the spectrum for sample 3. Sample 3 showed only the doublet contribution to the spectrum. As in samples 1 and 2, the spectrum was fit with Gaussian-broadened Lorentzian lineshapes to extract the electric hyperfine parameters, as indicated in Table 4.

Table 4 summarizes the analysis of the spectra. Here B_N is the nuclear hyperfine field (kG), 2ε the electric quadrupole shift (mm/s), δ_{Fe} the isomer shift relative to iron metal (mm/s), Γ the Lorentzian broadening (mm/s), and σ is the Gaussian broadening (mm/s). Values shown in parentheses were held fixed in the curve-fitting procedure. The area ratios of the II subspectra and I subspectra for the magnetic component are indicated I_{II}/I_I, and the total fraction of the absorption area under the magnetic subcomponent is indicated as $I_M/I_T = I_M/(I_D + I_M)$. The last column in Table 4 indicates the overall absorption of each sample, corrected for counting time and slight differences in sample

Table 4
Analysis of Möessbauer spectra for hyperfine parameters (B_N, nuclear hyperfine field (kG), 2ε, electric quadrupole shift (mm/s), δ_{Fe}, isomer shift relative to iron metal (mm/s), Γ, Lorentzian broadening (mm/s), and σ, Gaussian broadening (mm/s), I_{II}/I_I, area ratios of the II subspectra and I subspectra for the magnetic component, total fraction of the absorption area under the magnetic subcomponent, and $I_T/I_{T(3)}$, overall absorption of each sample, corrected for counting time and slight differences in sample masses, in ratio to sample 3

Oxides and sites	B_N (kG)	2ε (mm/s)	δ_{Fe} (mm/s)	Γ (mm/s)	σ (mm/s)	I_{II}/I_I	I_M/I_T	$I_T/I_{T(3)}$
Magnetite						1.85	1.00	–
I(A)	489	–	0.27	0.05[a]	0.05			
II(B)	458	–	0.66	0.15[a]	0.05			
Blank-EC in Fe–e (1)						0.85	0.07	1.8
D	–	0.69	0.34	0.18	0.10			
I	(489)	–	(0.27)	0.31[a]	(0.05)			
II	(458)	–	(0.66)	0.37[a]	(0.05)			
As-EC in Fe-EC (2)						0.74	0.52	5.6
D	–	0.59	0.36	0.17	0.08			
I	490	–	(0.27)	0.43[b]	(0.05)			
II	458	–	(0.06)	0.81[c]	(0.05)			
As-EC in Al-EC (3)	–	0.75	0.34	0.16	0.10	–	0.0	1.0

Values for 2ε, $\delta_{Fe,}$ Γ, and σ are in mm/s. Parameters in parentheses indicate values fixed in the least-squares fitting procedure.
[a] Linewidth indicated is for lines 1 and 6. Widths of other lines were assumed to be proportional to the relative magnetic shift for lines 2, 5 and 3,4.
[b] Linewidth indicated is for lines 1 and 6. Other line-widths were extracted in the least-squares procedure: $\Gamma_{25} = 0.34$ mm/s and $\Gamma_{34} = 0.14$ mm/s.
[c] Linewidth indicated is for lines 1 and 6. Other line-widths were extracted in the least-squares procedure: $\Gamma_{25} = 0.54$ mm/s and $\Gamma_{34} = 0.25$ mm/s.

masses, as a ratio with sample 3. This gives a measure of the relative amount of iron, per mg, in each sample.

Data for a stoichiometric magnetite sample (Fig. 14E) were obtained for comparison with samples 1 and 2. Electric hyperfine parameter values extracted from this spectrum were held fixed in the curve-fitting procedure for samples 1 and 2, and the B_N values were fixed for the I and II sites for sample 1. The values are in good agreement with literature values [56]: I (Fe^{3+} site, or A): $B_N = 491$ kG, $\delta_{Fe} = 0.28$ mm/s; II ($Fe^{2.5+}$ site, or B): $B_N = 460$ kG, $\delta_{Fe} = 0.66$ mm/s; relative intensity $I_{II}/I_I \sim 1.9$.

Note that the hyperfine magnetic field values extracted from sample 2 are also in good agreement with literature values for magnetite. The increased Lorentzian widths of the outer lines in both I and II sites in the magnetite components is probably a super-paramagnetic relaxation effect due to small particle sizes. Finally, the relative intensity of the II and I sites indicates the non-stoichiometric magnetite/maghemite (here II refers to the $Fe^{2.5+}$ site in the magnetite structure, which is absent in the stoichiometric endpoint maghemite, γ-Fe_3O_4, in which both the octahedral and tetrahedral sites are occupied by Fe^{3+} with a hyperfine field of about 500 kG [56]).

The isomer shift δ_{Fe} and quadrupole splitting 2ε obtained for the doublet component (D) in the three samples are consistent with iron oxyhydroxides (e.g., α-FeOOH, β-FeOOH, γ-FeOOH) in the form of very fine particles [57]. The relatively low absorption of sample 3 (last column in Table 1), may indicate aluminum substitution, reducing the iron content of the sample [58].

3.3. Ion-substitution in EC by-products

The incorporation of Fe^{3+} ions into amorphous/poorly crystalline aluminum hydroxide/oxyhydroxide and incorporation of Al^{3+} into amorphous/crystalline iron oxide/hydroxide/oxyhydroxide may play a significant role in the electrochemistry of removal of arsenic using a combined Fe–Al electrode system. The X-ray diffraction and Mössbauer spectroscopic results of the combined Al–Fe electrode system of our work suggests the ionic substitution of Fe^{3+} (ionic radius: 0.64 Å) by Al^{3+} (ionic radius: 0.50 Å), which may provide an alternative arsenic removal mechanism by electrocoagulation.

It has been found that substitution of Al cations for Fe ions in the iron oxide/hydroxide/oxyhydroxide generated during the EC process would slow down the transformation of amorphous iron oxide/hydroxide/oxyhydroxide species to crystalline phase [42]. In situ generated amorphous aluminum oxyhydroxide/hydroxide has resistance to redox reactions. Co-precipitation of poorly crystalline iron oxide/hydroxide/oxyhydroxide and amorphous aluminum species can most likely retard the transformation into crystalline species which possess very small surface area. Satapanajaru et al. [59] reported that because of its smaller ionic radius, isomorphous substitution of Al^{3+} for Fe^{3+} in iron oxides disrupts crystallization and results in a larger surface area of the total oxide mineral, which would increase adsorption. Exchangeable aluminum also increases Brønsted acidity by promoting reaction with water to release H^+ ions. Adsorbed Al can act as a Lewis acid by coordinating the moieties of some organic contaminants, bringing them closer to the iron oxide surface for reductive transformations. Other possible reactions include: mineral-catalyzed hydrolysis and oxidation. Both of these reactions involve complexation with surface Al^{3+} [60].

4. Summary

The use of dissimilar metallic electrodes, such as aluminum and iron, provides an alternative method for removal of arsenic from water by electrocoagulation. The frequent change of electrode-polarity may provide an efficient way for removal of both organic and metallic pollutants from water. In this study, the results of experiments with a wide range of arsenic concentration (1–1000 ppm) at different pH (4–10) have been presented and the removal efficiency of arsenic at these different conditions

has been discussed. XPS studies confirmed that during EC process As(III) ions are partly converted to As(V). Analysis of the solid adsorption product by PXRD, XPS, SEM/EDAX, FT-IR, and Mössbauer Spectroscopy revealed the expected crystalline iron oxides (magnetite, iron oxide), iron oxyhydroxide (lepidocrocite), aluminum hydroxide (bayerite), and aluminum oxyhydroxide (diaspore), as well as some interaction between the two phases. They also indicates the presence of amorphous or ultrafine particular phase in the floc. The observation of the substitution of Fe^{3+} ions by Al^{3+} ions in the solid surface indicates an alternative removal mechanism of arsenic in these metal hydroxides and oxyhydroxides. Al^{3+} substitution during formation of crystalline and/or amorphous/poorly crystalline Fe hydroxide/oxyhydroxides resulted in a product that might be more stable against transformation to well crystalline iron oxides.

Acknowledgements

We are greatly thankful for financial support from US Department of Agriculture (Award no. 2004-38899-02181), the U.S. Agency for International Development (TIES, Project no. 96860), and the Welch foundation (Grant no. V-1103). NSF Grant no. 0116153 was also essential for contributions toward the X-Ray Diffraction system. This material is based in part upon work supported by the Texas Advanced Technology Program under Grant No. 003581-0033-2003.

References

[1] M.Y.A. Mollah, R. Schennach, J.R. Parga, D.L. Cocke, Electrocoagulation (EC)-science and applications, J. Hazard. Mater. 84 (2001) 29–41.
[2] J.G. Hering, P.Y. Chen, J.A. Wilkie, M. Elimelech, Arsenic removal by ferric chloride, J. Am. Water Works Assoc. 88 (1996) 155–167.
[3] P.H. Masscheleyn, R.D. Delaune, W.H. Patrick, Effect of redox potential and pH on arsenic speciation and solubility in a contaminated soil, Environ. Sci. Technol. 25 (1991) 1414–1419.
[4] M. Pourbaix, Atlas of Electrochemical Equilibria in Aqueous Solutions, National Association of Corrosion Engineers, Texas, 1974, p. 520.
[5] V.E. Cenkin, A.N. Belevstev, Electrochemical treatment of industrial wastewater, Eff. Water Treat. J. 25 (7) (1985) 243–249.
[6] N. Biswas, G. Lazarescu, Removal of oil from emulsions using electrocoagulation, Int. J. Environ. Stud. 38 (1991) 65–72.
[7] R.R. Renk, Electrocoagulation of tar sand and oil shale wastewater, Energy Prog. 8 (1988) 205–208.
[8] S.H. Lin, C.F. Peng, Treatment of textile wastewater by electrochemical method, Water Res. 28 (1994) 277–282.
[9] S.H. Lin, M.L. Chen, Treatment of textile wastewater by chemical methods for reuse, Water Res. 31 (1997) 868–876.
[10] J.S. Do, M.L. Chen, Decolourization of dye-containing solutions by electrocoagulation, J. Appl. Electrochem. 24 (1994) 785–790.
[11] E.A. Vik, D.A. Carlson, A.S. Eikum, E.T. Gjessing, Electrocoagulation of potable water, Water Res. 18 (1984) 1355–1360.
[12] M.F. Pouet, A. Grasmick, Urban wastewater treatment by electrocoagulation and flotation, Water Sci. Technol. 31 (1995) 275–283.
[13] X. Chen, G. Chen, P.L. Yue, Separation of pollutants from restaurant wastewater by electrocoagulation, Sep. Purif. Technol. 19 (2000) 65–76.
[14] A.S. Koparal, U.B. Ogutveren, Removal of nitrate from water by electroreduction and electrocoagulation, J. Hazard. Mater. B 89 (2002) 83–94.
[15] F. Shen, X. Chen, P. Gao, G. Chen, Electrochemical removal of fluoride ions from industrial wastewaters, Chem. Eng. Sci. 58 (2003) 987–993.
[16] J. Mrozowski, J. Zielinski, Studies of zinc and lead removal from industrial wastes by electrocoagulation, Environ. Prot. Eng. 9 (1983) 77–85.
[17] J. Farkas, G.D. Mitchell, An electrochemical treatment process for heavy metal recovery wastewaters, AIChE Symp. Ser. 243 (81) (1985) 57–66.
[18] U.B. Ogutveren, N. Gonen, A.S. Koparal, Removal of chromium from aqueous solutions and plating bath rinse by an electrochemical method, Int. J. Environ. Stud. 45 (1994) 81–87.
[19] P.R. Kumar, S. Chaudhari, K.C. Khilar, S.P. Mahajan, Removal of arsenic from water by electrocoagulation, Chemosphere 55 (9) (2004) 1245–1252.
[20] M.Y.A. Mollah, P. Morkovsky, J.A. Gomes, M. Kesmez, J.R. Parga, D.L. Cocke, Fundamentals, present and future perspectives of electrocoagulation, J. Hazard. Mater. B 114 (2004) 199–210.
[21] R. Jose, Parga, L. David, Cocke, Ventura Valverde, A.G. Gomes Jewel, Mehmet Kesmez, Donald Mencer, Characterization of electrocoagulation for removal of chromium and arsenic, Chem. Eng. Technol. 28 (5) (2005) 605–612.
[22] M. Rebhun, M. Lurie, Control of organic matter by coagulation and floc separation, Water Sci. Technol. 27 (11) (1993) 1–20.
[23] B.A. Manning, S.E. Fendorf, S. Goldberg, Surface structures and stability of arsenic (III) on goethite: spectroscopic evidence for inner-sphere complexes, Environ. Sci. Technol. 32 (16) (1998) 2383–2388.
[24] L.M. Pierce, B.C. Moore, Adsorption of arsenite on amorphous iron hydroxide from dilute aqueous solution, Environ. Sci. Technol. 14 (2) (1980) 214–216.
[25] A.H. Khan, S.B. Rasul, A.K.M. Munir, M. Habibuddowla, M. Alauddin, S.S. Newaz, A. Hussam, Appraisal of a simple arsenic removal method for groundwater of Bangladesh, J. Environ. Sci. Health A 35 (7) (2000) 1021–1041.
[26] F.E. Stuart, Electronic water purification progress report on the electronic coagulator—a new device which gives promise of unusually speedy and effective results, Water Sewage 84 (1946) 24–26.
[27] C.F. Bonilla, Possibilities of the electronic coagulator for water treatment, Water Sewage 85 (1947) 21–45.
[28] W. Sanfan, Studies on economic property of pretreatment process of brackish water using electrocoagulation (EC) method, Desalination 82 (1–3) (1991) 359–363.
[29] K. Valeria, Kovatcheva, D. Marin, Parlapanski, Sono-electrocoagulation of iron hydroxides, Colloid Surfaces A: Physicochem. Eng. Aspect 143 (1–3) (1999) 603–608.
[30] C. Tsouris, D.W. DePaoli, J.T. Shor, M.Z.-C. Hu, T.-Y. Ying, Electrocoagulation for magnetic seeding of colloidal particles, Colloid Surfaces A: Physicochem. Eng. Aspect 177 (2/3) (2000) 223–233.
[31] O. Larue, E. Vorobiev, C. Vu, B. Durand, Electrocoagulation and coagulation by iron of latex particles in aqueous suspensions, Sep. Purif. Technol. 31 (2) (2003) 177–192.
[32] Mehmet Kobya, Orhan Taner Can, Mahmut Bayramoglu, Treatment of textile wastewaters by electrocoagulation using iron and aluminum electrodes, J. Hazard. Mater. 100 (1–3) (2003) 163–178.
[33] R.V. Drondina, I.V. Drako, Electrochemical technology of fluorine removal from underground and waste waters, J. Hazard. Mater. 37 (1) (1994) 91–100.
[34] N. Mameri, A.R. Yeddou, H. Lounici, D. Belhocine, H. Grib, B. Bariou, Defluoridation of septentrional Sahara water of North Africa by electrocoagulation process using bipolar aluminum electrodes, Water Res. 32 (5) (1998) 1604–1612.
[35] N. Mameri, H. Lounici, D. Belhocine, H. Grib, D.L. Piron, Y. Yahiat, Defluoridation of Sahara water by small plant electrocoagulation using bipolar aluminum electrodes, Sep. Purif. Technol. 24 (1/2) (2001) 113–119.
[36] Nafaâ Adhoum, Lotfi Monser, Decolourization and removal of phenolic compounds from olive mill wastewater by electrocoagulation, Chem. Eng. Process. 43 (10) (2004) 1281–1287.
[37] D.P. Avetisyan, A.S. Tarkhanyan, L.N. Safaryan, Electrofloatation-coagulation removal of carbon black from acetylene production wastewaters, Sov. J. water Chem. Technol. 6 (1984) 345–346.
[38] P.K. Holt, G.W. Barton, M. Wark, C.A. Mitchell, A quantitative comparison between chemical dosing and electrocoagulation, Colloids Surf. A 211 (2002) 233–248.
[39] A.I. Ivanishvili, V.I. Przhegorlinskii, T.D. Kalinichenko, Comparative evaluation of the efficiency of electrocoagulation and reagent methods of clarifying waste water, Sov. J. Water Chem. Technol. 9 (1987) 468–469.

[40] V.K. Syrbu, R.V. Drondina, A.M. Romanov, A.I. Ershov, Combined electroflotocoagulation apparatus for water purification, Elektronnaya Obrabotka Materialov (Electron Treat. Metals) (1986) 57–59.
[41] T. Picard, G. Gathalifaud-Feuillade, M. Mazet, C. Vandensteendam, Cathodic dissolution in the electrocoagulation process using aluminum electrodes, J. Environ. Monit. 2 (2000) 77–80.
[42] Y. Masue, R. Loeppert, T. Kramer, Adsorption, Desorption and Stabilization Behavior of Arsenic on Ferrihydrite and Al-substituted Analogs. Progress Report, Department of Soil and Crops Sciences, Texas A&M University: College Station, TX, 2004.
[43] J.B. Dixon, S.B. Weed (Eds.), Minerals in Soil Environments, 2nd ed., Soil Science Society of America, Madison, WI, 1989, pp. 331–378.
[44] http://www.mc.mat.shibaura-it.ac.jp/∼plaza/chap211.html, accessed in June, 2005.
[45] D.T. Harvey, R.W. Linton, Chemical characterization of hydrous ferric oxides by X-ray photoelectron spectroscopy, Anal. Chem. 53 (1981) 1684–1686.
[46] E.G. Sogaard, R. Aruna, J. Abraham-Peskir, C.B. Koch, Conditions for biological precipitation of iron by Gallionellaferruginea in slightly polluted ground water, Appl. Geochem. 16 (2001) 1129–1137.
[47] A.I. Zouboulis, I.A. Katsoyiannis, Recent advances in bioremediation of arsenic-contaminated ground waters, Environ. Int. 31 (2005) 213–219.
[48] S. Bang, M.D. Johnson, G.P. Korfiatis, X. Meng, Chemical reactions between arsenic and zero-valent iron in water, Water Res. 39 (2005) 763–770.
[49] S. Goldberg, C.T. Johnston, Mechanisms of arsenic adsorption on amorphous oxides evaluated using macroscopic measurements, vibrational spectroscopy, and surface complexation modeling, J. Colloid Interf. Sci. 234 (2001) 204–216.
[50] H.D. Ruan, R.L. Frost, J.T. Kloprogge, L. Duong, Infrared spectroscopy of goethite dehydroxylation: III. FT-IR microscopy of in situ study of the thermal transformation of goethite to hematite, Spectrochim. Acta Part A 58 (2002) 967–981.
[51] R. Balasubramaniam, A.V.R. Kumar, Characterization of Delhi iron pillar rust by X-ray diffraction, Fourier transform infrared spectroscopy and Mössbauer spectroscopy, Corros. Sci. 42 (2000) 2085–2101.
[52] A.V.R. Kumar, R. Balasubramaniam, Corrosion product analysis of corrosion resistant ancient Indian iron, Corros. Sci. 40 (7) (1998) 1169–1178.
[53] D.L. Cocke, E.D. Johnson, R.P. Merril, Planar models for alumina-based catalysts, Catal. Rev. Sci. Eng. 26 (2) (1984) 163–231.
[54] P. Bevington, Data Reduction and Error Analysis for the Physical Sciences, McGraw-Hill, New York, 1972.
[55] D.W. Marquardt, An algorithm for least-squares estimation of nonlinear parameters, J. Soc. Ind. Appl. Math. 11 (1963) 431.
[56] R.E. Vandenberghe, C.A. Barrero, G.M. da Costa, E. Van San, E. De Grave, Mössbauer characterization of iron oxides and (oxy)hydroxides: the present state of the art, Hyperfine Interact. 126 (2000) 247–259.
[57] H. Kodama, J.A. McKeague, R.J. Tremblay, J.R. Gosselin, M.G. Townsend, Can. J. Earth Sci. 14 (1977) 1–15.
[58] U. Schwertman, E. Murad, The influence of aluminum on iron oxides; XIV, Al-substituted magnetite synthesized at ambient temperatures, Clay Clay Miner. 38 (2) (1990) 196–202.
[59] T. Satapanajaru, S.D. Comfort, P.J. Shea, Enhancing metolachlor destruction rates with aluminum and iron salts during zerovalent iron treatment, J. Environ. Qual. 32 (2003) 1726–1734.
[60] M.B. McBride, Environmental Chemistry of Soils, Oxford Univ. Press, New York, 1994.